Femtosecond Real-Time Probing of Reactions. 20. Dynamics of Twisting, Alignment, and IVR in the *trans*-Stilbene Isomerization Reaction

J. S. Baskin, L. Bañares,[†] S. Pedersen, and A. H. Zewail*

Arthur Amos Noyes Laboratory of Chemical Physics, California Institute of Technology, Pasadena, California 91125

Received: March 26, 1996[⊗]

The femtosecond real-time dynamics of the isomerization reaction of *trans*-stilbene under collisionless conditions are studied using (2+1) resonance-enhanced multiphoton ionization (REMPI) and femtosecond depletion spectroscopy (FDS) in a pump−probe scheme. The observed transients reflect the macroscopic sample anisotropy decay (rotational coherence) and intramolecular vibrational energy redistribution (IVR) as well as the ethylenic twisting isomerization reaction. Polarization-resolved measurements are performed to isolate the influence of rotational dynamics, and the measured anisotropy decay is compared with theoretical calculations of rotational coherence at room temperature. The IVR and nonradiative (isomerization) processes of *trans*-stilbene are studied as a function of S_1 excess vibrational energy up to $\sim$6500 cm^{-1}. These results are compared with previous measurements of *trans*-stilbene under collisionless conditions and with predictions of RRK and RRKM theories.

I. Introduction

The isomerization reaction of *trans*-stilbene has been the subject of a wealth of experimental and theoretical studies during the last decades (for recent reviews, see refs 1 and 2). As shown schematically in Figure 1, the reaction in the excited state occurs by twisting of the ethylene bond toward a minimum on the potential energy surface (PES) at the $\theta = 90°$ configuration, referred to as the *phantom* state. From there, the population rapidly converts nonradiatively to the ground state surface. There is a barrier along the reaction path of 1200 $\pm$ 100 cm^{-1} ($\sim$3.4 $\pm$ 0.3 kcal/mol),[3] which results from an avoided crossing between the ^1B_u state and a doubly excited ^1A_g state.[4,5] For isomerization to take place, the excess vibrational energy deposited in nonreactive modes by an initiating light source must reach the reaction coordinate by intramolecular vibrational energy redistribution (IVR). This flow of population between modes is represented at the top left of Figure 1. Attention has been drawn to questions about the extent of IVR and the nature of the transition state as critical factors in the isomerization process by experimental observations of changes in the isomerization rate with isotopic substitution and in dense media. Numerous theoretical studies have shed light on this interesting problem.

In this laboratory, the focus has been on the dynamics of isolated *trans*-stilbene, substituted stilbenes, and stilbene van der Waals complexes cooled in supersonic beams. The nature of intramolecular vibrational energy redistribution (IVR),[6,7] time-dependent molecular alignment,[7−10] which may strongly influence the form of measured transients,[7] and twisting dynamics[3,11−13] have been investigated. The origin of IVR, the influence of structure on the twisting, and the relationship of rates in the isolated molecule to those in condensed media are issues of interest to these studies.

The general experimental methodology applied in this and other laboratories is illustrated in Figure 2. The *trans*-stilbene molecule is excited by a UV laser pulse of wavelength λ_1, and
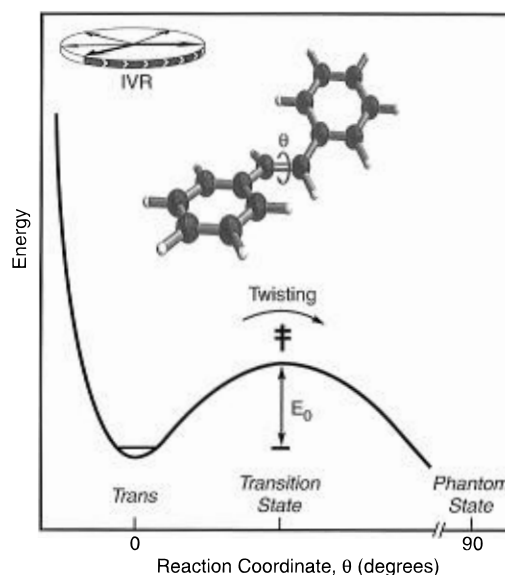

Figure 1. *trans*-Stilbene isomerization reaction. The *trans*-stilbene molecule is represented in the process of twisting about the ethylenic bond along the isomerization reaction coordinate θ. The potential curve represents schematically the excited state PES along θ from the *trans* configuration, through the transition state ‡, to the phantom state at $\theta = 90°$. At top left, vibrational excitation initially deposited in coordinates orthogonal to θ (leftmost heavy arrow) must redistribute by IVR to allow the reaction to proceed.

the temporal evolution of the resulting wave packet is probed by any one of a variety of techniques. Isomerization, IVR, and time-dependent molecular alignment (rotational coherence) have all been observed and thoroughly characterized by time-resolved laser-induced-fluorescence detection (LIF) in jet-cooled samples with low initial internal energies.[3,6,8,9,11−15] The time resolution in these experiments was tens of picoseconds. Both jet-cooled[7,10] and thermal samples[16] have been probed by resonance-enhanced two-photon ionization, while thermal samples have also been studied by picosecond transient absorption[17] and fluorescence up-conversion,[18] in each case with time resolutions of a few picoseconds. From these experiments, the excess energy dependence of the rate of isomerization, $k(E)$, has been

Femtosecond Real-Time Probing of Reactions

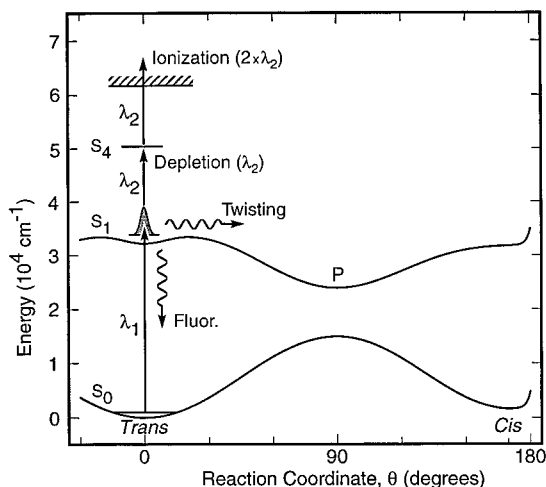*J. Phys. Chem., Vol. 100, No. 29, 1996* **11921**

Figure 2. General view of the potential energy for both the ground and excited states, depicting the methodology of the experiments. P is the perpendicular (phantom) state with minimum energy along θ in S_1. The initial preparation of the wave packet is by λ_1, and the probe process is either ionization by $2 \times \lambda_2$ or depletion of fluorescence by λ_2.

thoroughly characterized from 0 to ~ 3500 cm^{-1}, with limited additional data extending to 9000 cm^{-1}. The processes of IVR and rotational coherence have been well studied in a smaller energy range, principally in jet-cooled samples below 1330 cm^{-1}.

In this paper, femtosecond real-time studies using (2+1) resonance-enhanced multiphoton ionization (REMPI) and femtosecond depletion spectroscopy (FDS) are carried out on thermal samples to better characterize the dynamics in the high excess energy range. With time resolution an order of magnitude higher than used in previous studies, it is possible to resolve early time (<2 ps) transient evolution. This early time behavior is found to depend not only on the excess energy (pump wavelength) but on the technique used and the characteristics of the probe pulse. We relate these observations to the nature of IVR and rotational coherence, where the rotational dynamics can be separated from other processes by polarization selective probing. Isomerization occurs on a longer time scale, and its rate is measured from the decay of the slow component of the transients.

The outline of the paper is as follows. In section II, a brief description of the experiment and methodology is provided. A theoretical description of the kinetics of IVR and isomerization and of rotational coherence as applied in the analysis of our data is given in section III. The experimental results are presented and discussed in section IV, and comparisons are made to the predictions of theoretical models. Concluding remarks are given in section V.

II. Experimental Section

II.1. The Apparatus. The experimental apparatus has been described in detail elsewhere.[19] Briefly, the output of a colliding-pulse mode-locked laser (CPM) was amplified in four dye stages pumped by a 20 Hz Nd:YAG laser to yield pulses of 110−140 fs fwhm with energies up to 0.3 mJ and a central wavelength of 612 nm. The pulses were split into two arms of comparable intensity to provide the pump and probe lasers. For wavelengths other than the frequency-doubled fundamental of the CPM, the pump beam was tightly focused into a cell of D_2O to produce a white-light continuum, from which twice the desired pump wavelength was selected via a 10 nm bandpass interference filter. The transmitted light was further amplified

in a flowing dye cell which was end-pumped by residual Nd: YAG 532 nm radiation. The beam was then frequency doubled in a KD*P crystal to produce UV pump laser pulses. The pump laser pulses generated in this way had wavelengths in the range 270−330 nm. For probe wavelengths other than 610−612 nm, the same methods of white-light continuum generation and further amplification were used in the probe laser beam. Pulse widths of such pulses were typically 250−300 fs fwhm.

The probe pulse was propagated through a Michelson interferometer, in which its delay relative to the pump pulse was controlled by an actuator. The two beams were then collinearly recombined and focused into the reaction chamber (ionization or fluorescence). Fluorescence from laser-induced depletion experiments was collected perpendicular to the propagating beams and dispersed by a 0.33 m monochromator before being detected by a photomultiplier tube. The wavelength and bandwidth of the detected fluorescence were 330 and 7.2 nm, respectively, in the present experiments.

The *trans*-stilbene (Aldrich, 96%) was used as purchased without further purification. The sample was placed in the ionization or fluorescence chambers and evacuated to $\sim 10^{-5}$ Torr. All the ionization experiments were made at room temperature. The depletion experiments required higher *trans*-stilbene vapor pressures, and the fluorescence chamber was heated gently at typically 80 °C.

II.2. Methodology and Pulse Characterization. In the ionization experiments (see Figure 2), the temporal evolution of the wave packet created by a UV femtosecond laser pulse (λ_1) was probed by resonance-enhanced multiphoton ionization (REMPI), using two visible probe photons (λ_2) in a pump−probe scheme.[20] Care was taken to avoid high levels of multiphoton ionization background from each laser individually. The ionization background was reduced to low values by attenuating the pump and probe lasers using neutral density filters. In the polarization experiments, a polarizer was placed in the pump arm before doubling and another in the probe beam after a $\lambda/2$ plate. The polarization of both lasers was checked close to the focusing area.

Unlike the typical pump−probe experiment in which the excited state of interest, populated by the pump pulse, is probed to a different fluorescing or ionized state, which is the source of the measured signal, in the laser-induced depletion experiment, the fluorescence monitored is that of the state of interest itself. Thus, following excitation of *trans*-stilbene by the pump pulse, the subsequent fluorescence is depleted by the probe pulse (λ_2). By measuring the dependence of the fluorescence intensity on the relative delay between the pump and probe pulses, we directly monitor the dynamics of the molecule in the excited state. This method has been used in a previous publication from this laboratory.[21]

Autocorrelation and spectral measurements were made for several experiments in order to characterize the laser pulses. In addition, as in a previous publication,[21] I_2 transients were used as an internal calibration of the instrumental response function, as its shape is given by the cross correlation of the pump and probe profiles convoluted with an instantaneous rise and a long single-exponential decay function, reflecting the very long lifetime of I_2. In most cases, the appropriate instrument response function was determined by matching the *trans*-stilbene transient rise to a convolution of the assumed molecular response function (vide infra) with Gaussian trial functions of varying width.

III. Theory

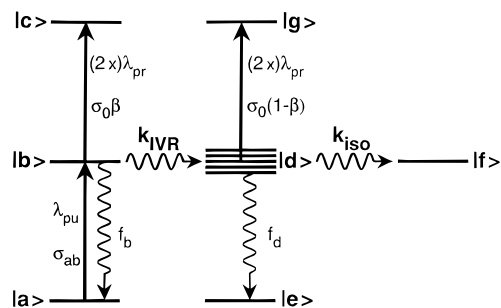**III.1 Dynamics of Twisting and IVR.** As represented schematically in Figure 1, IVR is a first step in the S_1 dynamics

Figure 3. Schematic of the kinetic model used to model the observed dynamics of *trans*-stilbene. λ_{pu} and λ_{pr} represent here the pump and probe pulses, respectively. k_{IVR} is the rate of intramolecular vibrational energy redistribution. k_{iso} is the isomerization or nonradiative decay rate. The f_i are the fluorescence rates from levels $|i\rangle$. β and σ_0 are used to express the difference in probe transition cross sections for the $|b\rangle$ and $|d\rangle$ levels and are defined in the text.

of *trans*-stilbene. Experimentally, the onset of IVR in the restricted form of fluorescence quantum beats is observed well below the isomerization barrier, at an excess energy of 396 cm^{-1},[22] and beating fluorescence is common between 663 and 1170 cm^{-1}.[6] IVR becomes dissipative (no major recurrences within the excited state lifetime of 2.7 ns) above 1200 cm^{-1},[6] near the energy of the isomerization barrier. Isomerization then occurs from an equilibrated bath of vibrational states with little or no mode dependence. No evidence for any other nonradiative process has been found, so that, after IVR, the *trans* population decays by a rate equal to the sum of the isomerization and fluorescence rates.

In many cases, transients measured in the dissipative IVR energy region are quasi-biexponential in form, reflecting the fast vibrational dephasing, followed by the slower *trans* depopulation by the isomerization reaction.[6−8,16] The representation of the dephasing process as an exponential decay is only an approximation, but provides a simple model for quantitative analysis. Figure 3 is a schematic representation of the energy levels and transitions that need to be considered in modeling the population flow in the molecule. With reference to Figure 3 (ignoring the upper tier of states $|c\rangle$ and $|g\rangle$ for the moment), we will make the following definitions: k_{IVR} = the rate of intramolecular vibrational redistribution, from state $|b\rangle$ to states $|d\rangle$; f_i = the rate of fluorescence from state $|i\rangle$; k_{iso} = the rate of isomerization from $|d\rangle$ to $|f\rangle$.

The initially prepared level $|b\rangle$ is coupled to the vibrational bath of states $|d\rangle$. In the LIF experiments,[6,8] fluorescence emission f_b and f_d, from $|b\rangle$ and $|d\rangle$, respectively, can be spectrally resolved, and the nature of the fast decay can therefore be confirmed as IVR by observing the decay of $|b\rangle$ and the buildup of $|d\rangle$. At the low excess energies of those experiments, the density of coupled states is not too high, and the reverse IVR rate is important. Thus $|b\rangle$ and $|d\rangle$ equilibrate with substantial population still in $|b\rangle$, resulting in observed biexponential decay of $|b\rangle$.[6,8] On the other hand, in pump−probe experiments such as those in this paper, $|b\rangle$ and $|d\rangle$ are probed simultaneously, with relative efficiencies dependent on the nature of the probe process. (While it is possible in principle to monitor either f_b or f_d in fluorescence depletion, in practice, the enormous difference between f_b and k_{IVR} makes the time-integrated fluorescence from $|b\rangle$ vanishingly small.) The measured signal is then a superposition of the two transient forms and may take on a variety of appearances, among which will be biexponential decays. The additional factor of time-dependent alignment on the initial decay is neglected for the moment, but will be considered in detail in the following subsection.

To relate the transients to the various rates for the pump−probe experiment, we can solve a simple kinetic model based on the scheme of Figure 3 in which transitions are treated in the linear response regime. Both the ionization and the fluorescence depletion transients are considered. The scheme and model are equivalent to those used in a previous work on methyl salicylate,[21] and the reader is referred to that work for additional details. The density of bath states at $|d\rangle$ is considered high enough to neglect the reverse IVR rate in the present analysis. Examination of the effect of reversibility in a kinetic model treatment of the LIF experiments can be found in ref 12

The number of molecules the pump excites from $|a\rangle$ to $|b\rangle$ is given by $n_0 = N\sigma_{ab}\lambda_{pu}E_{pu}/(hc\pi R^2)$, where N is the number of molecules in the interaction region, σ_{ab} is the pump absorption cross section, and the pump has wavelength λ_{pu} and total energy E_{pu} and is focused to radius R in the interaction region.

Considering next the probe step, β is defined as a dimensionless parameter describing the relative strength of the two possible probe absorptions such that $\beta\sigma_0$ = cross section for probing from state $|b\rangle$ to state $|c\rangle$, and $(1 - \beta)\sigma_0$ = cross section for probing from states $|d\rangle$ to state $|g\rangle$, where $0 \leq \beta \leq 1$, and σ_0 = a constant cross section.

With the chosen wavelengths in the present experiments, two photons are required from the probe pulse for ionization to occur and be detected. On the other hand, for the fluorescence depletion experiment one photon of the probe (to a resonant state) is enough to decrease the fluorescence, while two or more photons of the probe will, of course, also cause depletion, but to a lesser extent. Hence the two experiments, detecting ionization and monitoring fluorescence depletion, have different probing cross sections, and hence the probe cross section ratios (β: $1 - \beta$) for the two experiments will almost certainly differ. To indicate this distinction, the parameters σ_0 and β are replaced by σ_{0i} and β_i if the experiment is that of ion detection and σ_{0f} and β_f if the experiment involves detection of the fluorescence.

The general form of the solution to this model is discussed in the Appendix. Here, we present the solutions relevant to the situation at hand, which results from imposing the following simplifying restrictions:

$$k_{iso} + f_d \ll k_{IVR} \tag{1a}$$

$$f_b \ll k_{IVR} \tag{1b}$$

$$f_b/k_{IVR} \ll f_d/k_{iso} \tag{1c}$$

The last restriction is only invoked in the derivation of the fluorescence signal to ensure that the integrated fluorescence comes (almost) entirely from the vibrationally redistributed states, $|d\rangle$. When f_b and f_d are on the same time scale, eq 1c follows immediately from eq 1a. In the present case, limitation 1b is very well satisfied since f_b is on the nanosecond time scale, while k_{IVR} is on the subpicosecond time scale.

Solving for the populations of the various states, we obtain the expression for the molecular response as a function of the time delay, t, between pump and probe. The molecular response function is determined by the total number of molecules that are probed from $|b\rangle$ to $|c\rangle$ as well as the number probed from $|d\rangle$ to $|g\rangle$. For the ionization signal we obtain

$$M_{ion}(t) = 0, \quad t < 0 \tag{2a}$$

$$= n_0\alpha\sigma_{0i}[\beta_i \exp(-k_{IVR}t) + (1 - \beta_i)\{\exp(-(k_{iso} + f_d)t) - \exp(-k_{IVR}t)\}], \quad t \geq 0 \tag{2b}$$

where the constant α depends on the probe pulse. Similarly,

Femtosecond Real-Time Probing of Reactions

J. Phys. Chem., Vol. 100, No. 29, 1996 **11923**

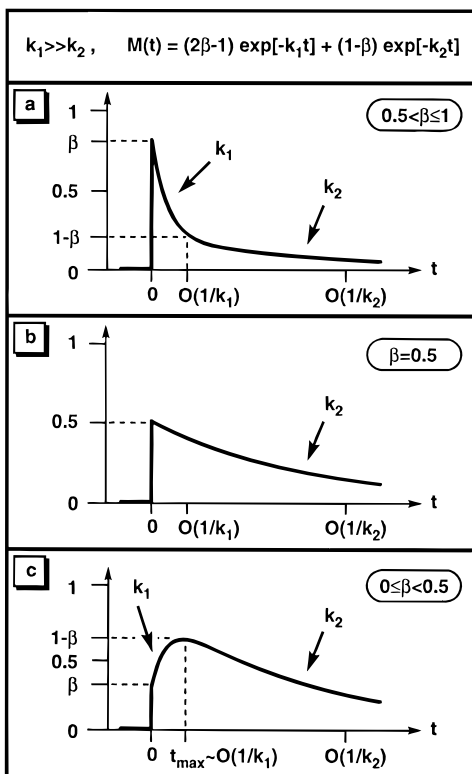**Figure 4.** Examples of transient temporal behavior according to eq 4 or 5, where $k_1 = k_{IVR}$ and $k_2 = k_{iso} + f_d$. Three cases are shown, representing the three basic forms that may occur, depending on the value of β.

for the normalized fluorescence signal response function we obtain

$$M_{fluor}(t) = 1, \quad t < 0 \tag{3a}$$

$$= 1 - \alpha\sigma_{0f}[\beta_f \exp(-k_{IVR}t) + (1 - \beta_f)\{\exp(-(k_{iso} + f_d)t) - \exp(-k_{IVR}t)\}], \quad t \geq 0 \tag{3b}$$

where the normalization factor is $n_0 f_d/(k_{iso} + f_d)$. Hence, the temporal evolution of the fluorescence signal would be of the same form as that of the ion signal were it not for the fact that β_f can be different from β_i. In the unsaturated regime, the effect of the finite laser pulse widths is incorporated through convolution of the molecular response with an appropriate instrument response function.

To explore the temporal behavior further, we write the respective response functions as follows:

$$M_{ion}(t) = 0, \quad t < 0 \tag{4a}$$

$$= n_0 \alpha\sigma_{0i}[(2\beta_i - 1) \exp(-k_{IVR}t) + (1 - \beta_i) \exp(-(k_{iso} + f_d)t)], \quad t \geq 0 \tag{4b}$$

and

$$M_{fluor}(t) = 1, \quad t < 0 \tag{5a}$$

$$= 1 - \alpha\sigma_{0f}[(2\beta_f - 1) \exp(-k_{IVR}t) + (1 - \beta_f) \exp(-(k_{iso} + f_d)t)], \quad t \geq 0 \tag{5b}$$

The dependence on β of the common temporal behavior expressed by eqs 4 and 5 is shown in Figure 4, where $k_1 = k_{IVR}$ and $k_2 = k_{iso} + f_d$. This behavior holds when the assumptions stated in eq 1 are satisfied. In that case, the $k_{iso} + f_d$ component

is always the slow decay (positive amplitude), while the component with the rate k_{IVR} can be either a rise (negative amplitude) or a decay, depending on whether β is less than or greater than 0.5, that is, on whether the cross section for probing $|d\rangle$ or for probing $|b\rangle$ is greater. If the two cross sections are equal ($\beta = 0.5$), the decay approaches a single exponential with rate $k_{iso} + f_d$. (The rates shown in Figure 4 are for illustration only, as they are too close in magnitude to make eq 1a a good approximation. The only consequence of k_1 and k_2 being close is to shift the value of β corresponding to single-exponential behavior slightly above 0.5.)

III.2. Dynamics of Alignment. By pumping an initially isotropic sample with a linearly polarized light pulse, a well-defined alignment of the excited state population is created. Subsequent interaction with a polarized probe will exhibit a polarization anisotropy associated with that alignment, which depends on the directions in the molecular frame of the pump and probe transition dipoles and evolves in time as a consequence of molecular rotation. The time dependence of this anisotropy, referred to as rotational coherence, has been treated theoretically for a variety of cases, both quantum mechanically and semiclassically,[23] and the general features of the theory have been confirmed by experimental observations on a variety of molecules, including *trans*-stilbene under jet-cooled conditions.[8-10] In this section, we will present the theoretical framework and assumptions used to model the time evolution of molecular alignment relevant to the current experiments.

It is known from previous polarization-resolved ionization measurements of jet-cooled *trans*-stilbene at the S_1 origin,[10] using the same two-photon ionization scheme employed in the present work, that rotational coherence takes a form very similar to that of a one-photon parallel-polarized transition. This is believed to be due to the fact that the polarization selectivity is determined by the first step in the probe sequence to the S_4 resonant intermediate and that the ionization step ($S^+ \leftarrow S_4$) is only weakly polarized. Therefore, in the following treatment, equivalence to a one-photon probe process will be assumed.

For the jet-cooled molecule ($T_{rot} \approx 2$ K, where T_{rot} is the sample rotational temperature), a full quantum mechanical treatment of *trans*-stilbene as a rigid asymmetric top, with coincident transition dipoles at a small angle from the a inertial axis, was used to reproduce the recurrence behavior in fluorescence.[9] Rotational eigenstates with total rotational angular momentum quantum number, J, up to ~40 were required for these calculation. Since the computational requirements for such a calculation scale as J^4, or T^2_{rot}, in this work, where calculations were performed for samples at $T_{rot} \approx 295-353$ K, only the much quicker symmetric top treatments were used. Both semiclassical and quantum calculations were carried out. For the early time behavior considered here, the restriction to symmetric top motion is inconsequential. The *trans*-stilbene anisotropies derived from quantum mechanical calculations with transition dipoles along the a axis, and from semiclassical calculations with coincident pump and probe dipoles at an angle of 10° with the a axis, were also effectively equal at early time. Small differences only appear beyond 3 ps, reaching a maximum difference of 0.073 *vs* 0.067 for the long time (>25 ps at 295 K) asymptotic, or residual, anisotropy. All calculations were for a rigid symmetric top with rotational constants $A = 2.6$ GHz and $B = 0.2566$ GHz, close to those of S_1 *trans*-stilbene.[9,24]

Whether the single molecule rotational quantum beats, which form the basis of rotational coherence, are treated quantum mechanically or classically, the macroscopically observable signals depend fundamentally on the nature of the ensemble average, which we address next. In analogy with the notation

of ref 25, we label distinguishable dynamic states by the index i, their populations (assumed isotropically distributed in the laboratory frame) by P_i, and the temporally dependent pump–probe signal from all molecules in that population, neglecting orientation dependent factors, by $a_i(t)$. Distinguishable dynamic behaviors include differing J or K (but not m), as well as differing vibronic state evolution. The magic angle signal, I_m, measured with pump and probe polarizations at 54.7°, is given by

$$I_m(t) = \sum_i P_i a_i(t) \tag{6}$$

and is thus free of alignment effects. The macroscopic polarization anisotropy, defined by

$$r(t) = (I_\parallel - I_\perp)/(I_\parallel + 2I_\perp) \tag{7}$$

where $I_\parallel$ and $I_\perp$ are the measured intensities of the signal with pump and probe polarizations parallel and perpendicular, respectively, is equal to

$$r(t) = \left(\sum_i P_i a_i(t)\, r_i(t)\right)/\left(\sum_i P_i a_i(t)\right) \tag{8}$$

Here $r_i(t)$ depends only on the rotational dynamics of the population P_i and is given classically by

$$r_i(t) = 0.4 P_2(\cos \eta(t)) \tag{9}$$

where $P_2(x)$ is the second-order Legendre polynomial, and $\eta(t)$ is the angle between the probe transition dipole at time t and the pump transition dipole at time $t = 0$. The analytical expressions needed to calculate $\eta(t)$ for classical rotation of a symmetric top are given in ref 25. The parallel and perpendicular transients may be calculated from $r(t)$ by

$$I_\parallel = [1 + 2r(t)]I_m(t) \tag{10a}$$

$$I_\perp = [1 - r(t)]I_m(t) \tag{10b}$$

where the vectorial alignment contributions are contained in the bracketed terms, and $I_m(t)$ represents all population dynamics.

In the simplest model, $a_i(t)$ does not depend on i, and eq 6 implies that all populations are characterized by a common temporal evolution $A(t) \propto I_m(t)$. In that case, $r(t)$ is given directly by the Boltzmann-weighted sum of the $r_i(t)$'s and thus depends only on the rotational dynamics of the sample, i.e. reflects purely rotational coherence. Moreover, $r(t)$ remains independent of the $a_i(t)$'s as long as there is no correlation between vibronic state evolution and rotational motion, since one may group the summation in eq 8 into populations with different $a_i(t)$'s but equal rotational state distributions. Even in these cases, however, it should be noted that the anisotropy derived from transients reflecting the consequences of limited temporal resolution, designated by $R(t)$, may depend weakly on $a_i(t)$, or $A(t)$, through convolution with the system response. Simulations of $R(t)$ are therefore produced by applying eq 7 to the simulated parallel and perpendicular decays, which are in turn derived from $r(t)$ by eq 10.

Only when different $a_i(t)$'s are associated with different rotational distributions does one expect a deviation of $r(t)$ from the form of purely rotational coherence. For example, a difference in rotational distributions in different product channels was postulated as the source of an unusual anisotropy decay following dissociation of HgI_2.[25] A corresponding situation

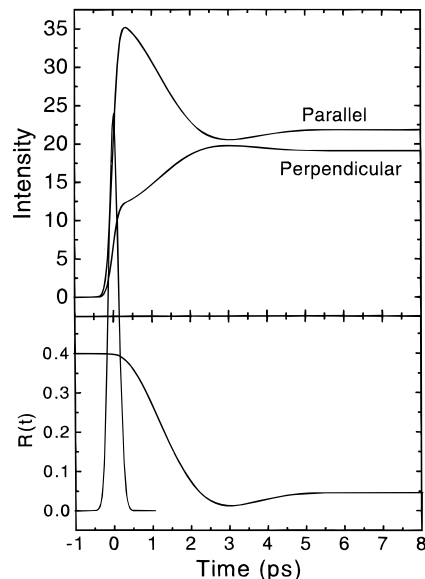**Figure 5.** (upper) Simulated polarization-resolved *trans*-stilbene transients for $T_{rot} = 295$ K: parallel and perpendicular polarizations; (lower) corresponding instrument response function and polarization anisotropy, $R(t)$. The rotational coherence is calculated quantum mechanically for parallel-polarized transitions of a symmetric top. $A(t)$ is a step function.

would apply in the present analysis, if the rate of any dynamic process were influenced by rotational motion.

Some examples of the effects of rotational coherence are shown in the following figures. The rotational coherence calculations, both quantum mechanical and classical, are appropriate to the *trans*-stilbene molecule at $T_{rot} = 295$ K, as described above. First, in the upper panel of Figure 5 is shown the form taken by transients for parallel and perpendicular probing of a metastable excited state prepared by the pump pulse; that is, $A(t)$ is a step function on the time scale of interest. Also shown in the lower panel is the system response function used (294 fs fwhm) and the resulting anisotropy.

Given the fact that the time evolution of transient features scales as $1/\sqrt{T_{rot}}$, where T_{rot} is the sample rotational temperature,[26,27] the anisotropy decay here is about a factor of 10 shorter than in molecular beam experiments. Nevertheless, by using a subpicosecond instrument response time, the rotational dynamics can be fully resolved. This fact is most easily recognized by the fact that $R(t)$ does not drop significantly from the limiting value of $r(0) = 0.4$ until after the experimental time zero, defined as the center of the symmetric instrument response. With such resolution, the effect on the appearance of the transients is quite dramatic. Depending on the signal-to-noise of the measurements, the observation of transients of this form might be misinterpreted as a rise or decay resulting from an intramolecular population transfer process, rather than from the actual dephasing of molecular alignment only. For example, the perpendicular transient of Figure 5 fits reasonably well to a biexponential form with a partial rising component of ~1.5 ps lifetime, even though there is no dynamic process other than rotation at play. At high S/N, however, the characteristic dip in the anisotropy, here at around 3 ps, is visibly imprinted on both the parallel and perpendicular transients.

As a second illustration of the effect of rotational coherence, consider a situation corresponding to the kinetic model discussed in section III.1. Two populations are probed, one for which $a_i(t)$ for all rotational states decays at the rate k_{IVR} and one for which $a_i(t)$ rises at that rate and decays at the rate $k_{iso} + f_d$. For the representative set of values given in Figure 6 and caption,

Femtosecond Real-Time Probing of Reactions

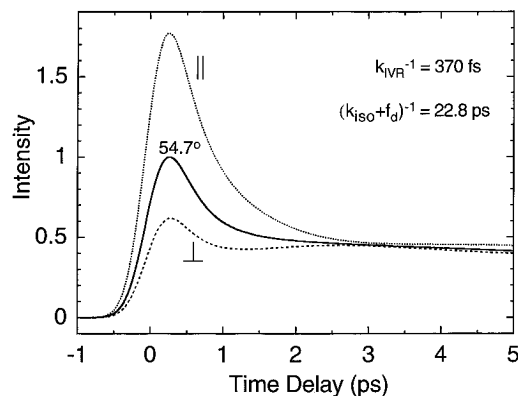*J. Phys. Chem., Vol. 100, No. 29, 1996* **11925**

Figure 6. Simulated polarization-resolved *trans*-stilbene transients: parallel, magic angle, and perpendicular polarizations. The rotational coherence was calculated classically for coincident transition dipoles 10° from the symmetric top figure axis. $A(t)$ has two components: a fast decay of lifetime 370 fs and a slow decay of 22.8 ps with fast to slow amplitude ratio 2.46/1 ($\beta = 0.776$). A Gaussian instrument response of 530 fs fwhm is used.

and with $\beta = 0.776$, one finds the transient behaviors shown (Figure 6) for parallel, magic angle, and perpendicular probe polarizations. The magic angle transient is the direct superposition of the two a_i's, uninfluenced by rotation. Since it was assumed that all rates are independent of rotational state, the discussion above indicates that the same $r(t)$ (ignoring the slight effect of classical *vs* quantum calculation) underlies the simulations of both Figure 5 and Figure 6, and it is found that $R(t)$ calculated from the Figure 6 transients differs negligibly from that plotted in Figure 5, despite the different response function and different $A(t)$. In Figure 6, the short decay component continues to be visible for each of the three polarizations represented, but with apparent amplitudes that depend strongly on polarization. In addition, due to a difference in time scales for the anisotropy decay and the IVR process, the perpendicular transient still shows a noticeable recurrence in intensity, although slightly shifted to around 2.7 ps.

IV. Results and Discussion

The femtosecond dynamics of the excited state of *trans*-stilbene were obtained by monitoring the ion or fluorescence signal as a function of time delay. Transients were measured for several excess vibrational energies changing the pump laser wavelength. Polarization measurements were also made.

Throughout, we shall use a shorthand notation to indicate the pump and probe wavelengths and detection mode in both ionization and depletion experiments. For the ionization experiments, we will use $\lambda_{pump}/\lambda_{probe}$(detection). For instance, 306/2×612(ions) means that *trans*-stilbene is initially excited with a 306 nm pump laser and then probed by REMPI with two photons of 612 nm and that ions are the detected species. For the depletion experiments, we will use $\lambda_{pump}/(\lambda_{detection})/\lambda_{probe}$. For instance, 306/(330)/612 means that *trans*-stilbene is initially excited with a 306 nm pump laser, and the subsequent fluorescence of the excited state at 330 nm is depleted with the 612 nm probe laser.

IV.1. The Effect of Alignment. We first examine the effect of alignment dynamics on the ionization transients. For this purpose, experiments were carried out with well-determined pump and probe polarizations. Measurements were made for parallel, perpendicular, and magic angle (54.7°) polarizations, as indicated in section II.2, and as expected, the shape of the transient was found to depend on the relative polarization of the pump and probe laser pulses. Figure 7 shows an example
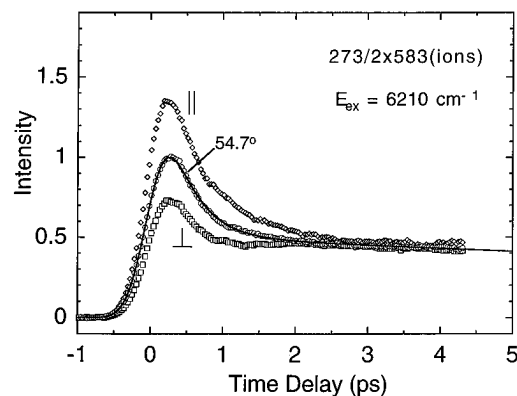

Figure 7. Effect of the relative polarization of pump and probe pulses on the experimentally measured 273/2×583(ions) transient. The fit to the data corresponding to magic angle polarization is identical to the magic angle simulation of Figure 6.
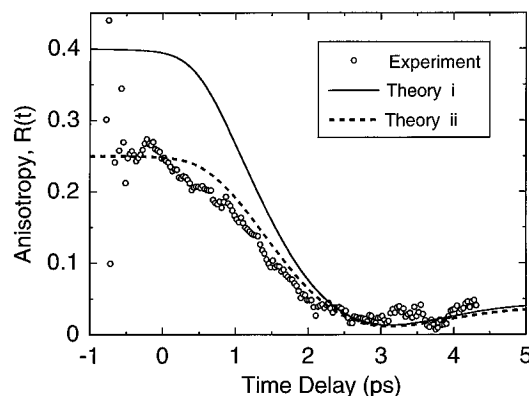

Figure 8. Experimental polarization anisotropy $R(t)$ formed from the transients of Figure 7, compared with two simulations of $R(t)$ (theory i and theory ii) as described in the text. $A(t)$ and the instrument response for both calculations are as for Figure 6. Theory i is a quantum mechanical calculation with both transition dipoles along the a inertial axis, while theory ii is a classical calculation with transition dipoles in the molecular plane forming angles of +11° and −19° with that axis.

of transients measured for the three different polarizations and the pump−probe sequence 273/2×583(ions). The experimental anisotropy, $R(t)$, calculated from the transients of Figure 7 is plotted in Figure 8. Two simulations (see section III.2) of $R(t)$ are also shown in Figure 8, and will be discussed below. The alignment-independent molecular response ($A(t)$) for the calculations is derived from a fit of the magic angle data to a biexponential function.

As will be explained below, it was found that the shape of the transients depends on factors other than polarization, such as probe power, which were not systematically monitored in these experiments. Therefore, the relative normalization of the various polarizations is only approximate, and the quantitative characteristics of $R(t)$ are not precisely determined from these experiments. However, by choosing the normalization of parallel and perpendicular transients to match the experimental and theoretical values of $R(t)$ near the end of the experimental time range, as was done in Figure 7, the early time behavior of the anisotropy was found to be reproducible in experiments on different days. It is also evident from the comparison of theory and experiment in Figure 8 that the time scale of the measured anisotropy decay is in good agreement with theoretical expectations.

The $R(t)$ simulation in Figure 8 with early time asymptote of 0.4 (theory i) is formed from the theoretical transients previously discussed and shown in Figure 6. The magic angle transient from Figure 6 is replotted in Figure 7, and the scales of the two

11926 *J. Phys. Chem., Vol. 100, No. 29, 1996*

Baskin et al.

figures are identical. It is evident from a comparison either of the transients in these figures or of the corresponding $R(t)$'s in Figure 8 that the experimental anisotropy at early time is considerably lower than theory predicts. The same observation applies to measurements made by the same technique at zero excess energy in the molecular beam.[10] It can also be noted in Figure 7, where the scaling of parallel and perpendicular transients is chosen to reproduce the theoretical long time residual anisotropy, that the magic angle decay is not proportional to $I_\parallel + 2I_\perp$. Due to experimental variability in the characteristics of the biexponential transients (vide infra), especially the relative amplitudes of the fast and slow components, these observations cannot be well quantified. In passing, we note only that discrepancies between theory and experiment would not be surprising, given the approximation of the two-photon probe as a one-photon transition with transition dipole coincident with the transition dipole of the $S_1 \leftarrow S_0$ transition. In this treatment, both the alignment sensitivity of the second probe photon and possible differences between the $S_4 \leftarrow S_1$ and $S_1 \leftarrow S_0$ transition dipoles are neglected.

To illustrate one way in which the treatment might be modified to produce a lower initial anisotropy, a second simulation of $R(t)$ was carried out changing only the direction of the $S_4 \leftarrow S_1$ transition dipole by 30°. For this simulation, the pump and probe transitions were chosen to have dipoles aligned along the two symmetry axes of the phenyl rings which are closest in direction to and on opposite sides of the *a* principal inertial axis of the *trans*-stilbene molecule, at angles of +11° and −19°, respectively. (The positive sign here indicates increasing angular separation from alignment with the ethylene C=C bond.) These assumptions are consistent with all experimental observations.[9,24] The result is shown as a dashed line (theory ii) in Figure 8 and reproduces the data rather well.

In a previous measurement of time-resolved polarization anisotropy in hot (463 K) *trans*-stilbene vapor by fluorescence up-conversion,[18] the fact that the early time anisotropy was also quite low (<0.2) could be attributed largely to limited temporal resolution. There, the same transition dipole mediated both pump and probe steps, in which case $r(0)$ is necessarily 0.4. As the simulations show here, the temporal resolution of the present experiments is sufficient to yield directly the true early time asymptotic value of $r(t)$, provided the relative intensities of the transients can be accurately established.

The polarization-resolved experiments allow us to reach the following essential conclusions. First, the anisotropy decay occurs on the expected time scale. This decay being much longer than the instrument response function, the measured decay directly displays the alignment dynamics of the sample. The decay is determined by the rotational temperature and thus should be comparable in all our experiments. Second, the biexponential form persists at all probe polarizations and is therefore clearly not purely an alignment effect, but must reflect an internal dynamic process.

In all subsequent measurements to be discussed, polarizers were not used to define the polarizations of pump and probe beams, most of which were produced by continuum generation. The progenitor pulses for pump and probe were mutually perpendicular, but the resulting transients do not generally display the distinct nonexponentiality associated with perpendicular transients (see Figure 7). In particular, experiments at the same wavelengths (273/2×583(ions)) but without polarizers (as, for example, in Figure 11b) produced transients without the weak recurrence readily evident upon inspection of the perpendicular polarization transient in Figure 7. In addition, differences between the decay parameters of these transients

TABLE 1: Measured Decay Parameters for *trans*-Stilbene Ionization Transients[a]

E_{ex} (cm^{-1})	λ_{pump} (nm)	λ_{probe} (nm)	τ_{slow} (ps)	τ_{fast} (fs)	a_f	Figure
1830	310	2 × 583	*b*	780	0.88	14a
2250	306.1	2 × 612	250	25, 112	2.5, 0.4	9, 11a, 12
3120	306.1	612(depletion)	*b*	rise 65	−1	13
3640	293.6	2 × 612	88			9
4700	284.8	2 × 612	47			9
5300	280	2 × 580	37	650	0.83	
5620	277.5	2 × 612	32			9
6210	273	2 × 583	26	400, 560	2.1, 1.0	11b, −
6210^c	273	2 × 583	24	418	1.3	
6210^c	273	2 × 583	23	370	2.5	7
6480	271	2 × 583	22−25	450, 280	1.3, 2.5	14a, −

[a] Fast and slow lifetimes were not necessarily measured in the same transients. [b] The time scale of the experiment was too short to determine the slow component lifetime. [c] Magic angle.
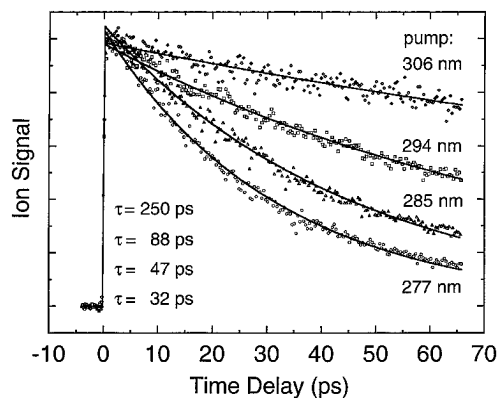

Figure 9. Ionization transients showing the dependence on the pump wavelength of the decay lifetime, τ, of the slow component. The probe wavelength was fixed at 612 nm.

and parameters derived from magic angle measurements are not greater than the intrinsic variability of such parameters. We attribute this to a low degree of polarization of the continuum light which effectively damps alignment selectivity. Rotational coherence may then be neglected in the following analysis without major consequence. Specifically, derived lifetimes of decay components well outside of the confirmed time scale of 1−2 ps for the anisotropy decay will not be fundamentally affected by any residual effect of probe polarization.

IV.2. Ionization *vs* Fluorescence Depletion Transients. Ionization and fluorescence depletion transients were obtained for different excess vibrational energies, changing the pump laser wavelength from 310 to 271 nm. The decay curves from ionization experiments may have one or two exponential decay components or a rise and a decay. Transients obtained using the fluorescence depletion technique show only a single decay component, with a rise detected in one case.

To analyze the early time behavior of the ionization data, transients of 1.5−12 ps in length were fit to a biexponential decay function with convolution, as described in section II.3. The lifetimes obtained in the fitting procedure are listed in Table 1. For a number of excess vibrational energies, transients were also obtained (see Figure 9) on a long time scale to more accurately determine the decay rate of the slow component. The excess vibrational energies listed in Table 1 were calculated knowing the *trans*-stilbene 0−0 transition energy (at λ = 310.14 nm)[12] and the thermal energy at the temperature of interest (23 °C for ionization and 80 °C for fluorescence depletion). The thermal energy was estimated using the method described in ref 21 and the 72 ground state vibrational frequencies calculated by Warshel,[28] with experimental corrections to the important

Femtosecond Real-Time Probing of Reactions

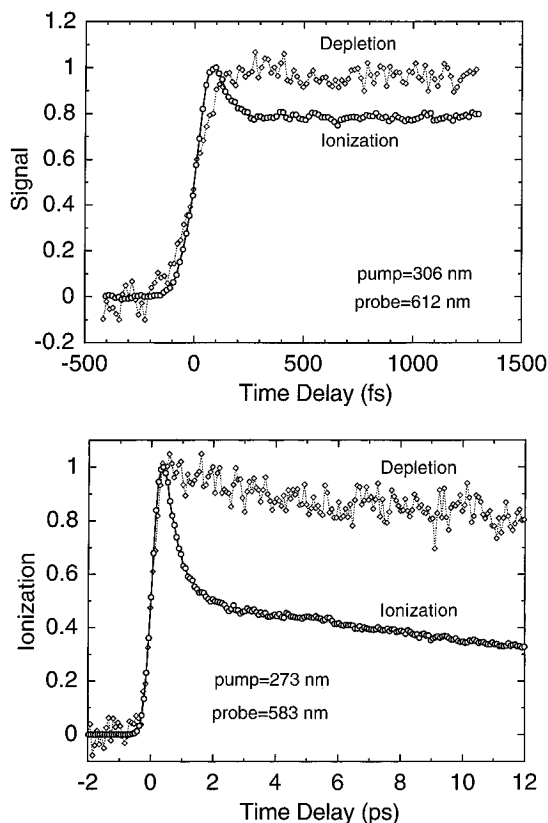*J. Phys. Chem., Vol. 100, No. 29, 1996* **11927**

Figure 10. Comparison of ionization and fluorescence depletion data. (a, top) Femtosecond transients obtained from the experiments with λ_1=306 nm and λ_2=612 nm. The ionization transient shows a biexponential with both a fast and a slow component in the decay. The depletion transient, however, has a fast component in the rise and a slow component in the decay. (b, bottom) Femtosecond transients obtained from the experiments with λ_1=273 nm and λ_2=583 nm. The ionization transient shows a biexponential with both a fast and a slow component in the decay. The magnitude of the fast component is very large for this high-energy probe. The depletion transient exhibits only a slow component in the decay.

low-frequency modes as summarized by Urano et al.[29] For example, for 23 °C, an average thermal energy of 1828 cm^{-1} was found.

Figure 10 contrasts the early time behavior of *trans*-stilbene transients obtained using ionization and depletion techniques for two different sets of pump–probe wavelengths. The results of the fits of the ionization data, along with the derived short lifetimes, are shown in Figure 11. When pumping to an energy of 2250 cm^{-1} and probing at 612 nm (Figure 11a), the fast component is faster than the 150 fs instrument response (as derived from I$_2$ transients), while pumping at an energy of 6210 cm^{-1} and probing at 583 nm (Figure 11b) gives a much slower fast component, comparable in length to the instrument response appropriate for that experiment (note the different time scales). In both cases, a range of values (see Table 1) have been measured for the fast component lifetime and for a_f, the fast to slow component amplitude ratio, with the amplitude ratio increasing at higher probe power. Figure 12 shows the effect on the fast component of 306/2×612(ions) transients for different probe intensities. On the other hand, for the fluorescence depletion transients in Figure 10, no fast decay component is detectable for either probe wavelength. However, the depletion data of Figure 10a is best fit with an exponential buildup with a 65 fs lifetime. The fit is shown in Figure 13, with the instrument response again based on I$_2$ transients.

For the 583 nm probe ionization experiments, the measured fast lifetimes decrease from ~800 to ~350 fs as the pump
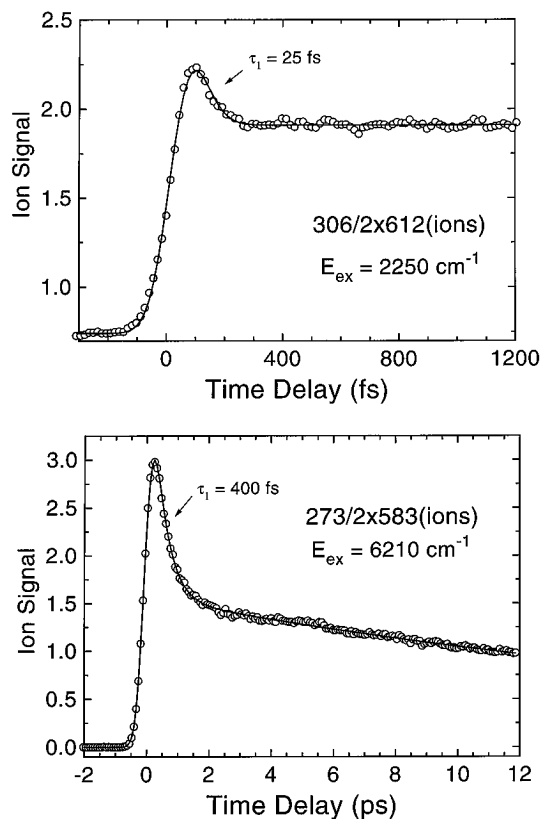

Figure 11. Fits of the ionization data in Figure 10. (a, top) 306/2×612-(ions) experimental transient (circles) and a biexponential fit to the data. The fit has fast and slow components in the decay having lifetimes of 25 fs and ~250 ps, respectively. The fwhm of the cross correlation deduced from I$_2$ transients is 150 fs. (b, bottom) 273/2×583(ions) experimental transient (circles). The biexponential fit has fast and slow components in the decay with lifetimes of 400 fs and 25 ps, respectively. A cross correlation of 515 fs fwhm was used to fit the rise of the signal.
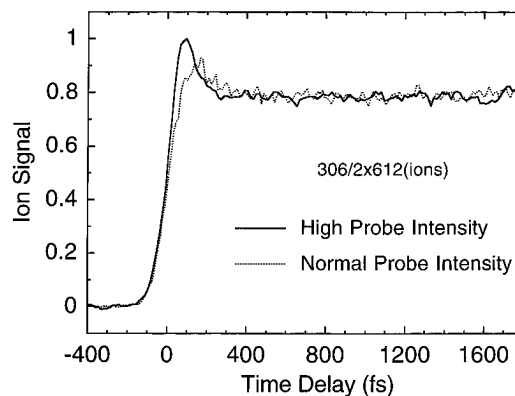

Figure 12. Effect of the probe intensity on the ratio of the magnitude of the fast to the slow component of the biexponential ionization transients in the 306/2×612(ions) experiment. The fast component lifetimes derived from fits to the data also differ as shown in Table 1.

energy is increased. Figure 14a shows examples of ionization transients with a 583 nm probe but different pump energies. For the high-energy pump (271 nm) the decay rates for both the fast and the slow component of the biexponential are larger than for the lower energy pump (310 nm). The effect of changing the probe energy from 583 to 612 nm is illustrated in Figure 14b. When probing at 612 nm, no fast component is seen except for the 306 nm pump experiments (Figure 10a), and the derived lifetime in that case is on a much shorter time scale.

IV.3. IVR. As in other cases of biexponential decay kinetics of *trans*-stilbene (with proper consideration of rotational coher-
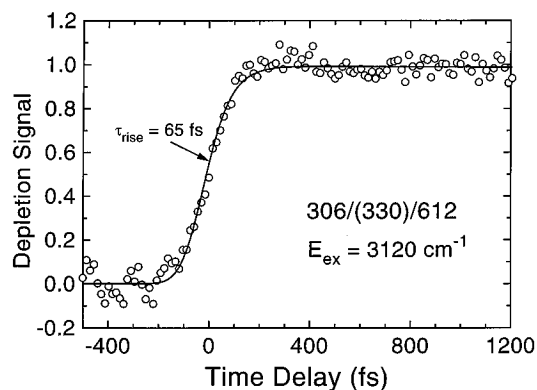
Figure 13. Femtosecond fluorescence depletion transient, 306/(330)/612. The smooth line is the result of a fit with a fast component in the rise (65 fs) and a slow component in the decay much longer than the time scale of the experiment. The fwhm of the cross correlation deduced from I_2 transients is 150 fs.
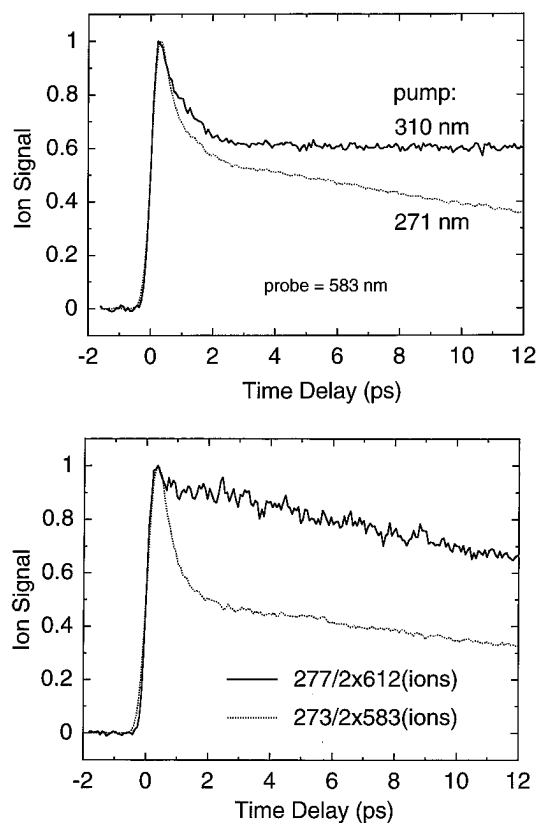

Figure 14. (a, top) Ionization transients showing the effect of varying the pump. The probe was fixed at 583 nm, and the two transients correspond to pump wavelengths of 310 and 271 nm. Both transients are biexponential; both rates for the 271 nm excitation are faster than the corresponding rates for the 310 nm case. (b, bottom) Ionization transients showing the probe wavelength dependence. Transients are shown for the 277/2×612(ions) and 273/2×583(ions) experiments. The higher the energy of the probe, the larger the magnitude of the fast component.

ence, as already discussed), the fast decay component in our measurements is associated with IVR. This identification is supported by the kinetic model analysis (see the Appendix). In addition to the present results, as presented in Table 1, it is pertinent also to consider the room temperature bulb measurements of ref 16. There, the same ionization scheme was employed with ~3 ps pulses, and a 2 ps fast component was observed at all excess energies from 1800 to 4400 cm^{-1}. First, it is instructive to have an estimate of the expected behavior of the IVR rate as a function of excess energy.
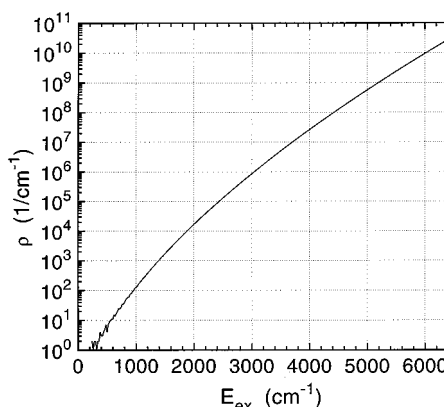

Figure 15. Vibrational density of states of *trans*-stilbene *vs* energy, by direct count. Vibrational modes are assumed harmonic, with frequencies for the fundamentals taken from refs 28 and 29.
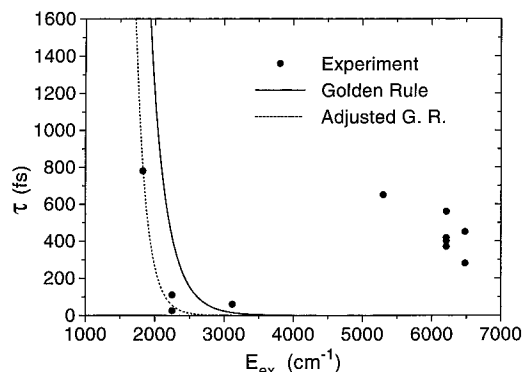

Figure 16. Measured IVR lifetimes as a function of excess energy. The solid curve is an extrapolation from picosecond rates by means of eq 11 and the calculated density of vibrational states shown in Figure 15. The dashed line is an adjustment of the solid curve to pass through the measured value of $\tau_{IVR} = 780$ fs at 1830 cm^{-1} (see text).

From molecular beam studies,[6,8] IVR lifetimes of 25−45 ps, depending on the mode excited, are reproducibly measured between 1230 and 1330 cm^{-1} excess energy in S$_1$ *trans*-stilbene, with excitation by pulses of <15 ps duration. These rates therefore are taken as accurate reflections of the spread of the zeroth-order mode character among the molecular eigenstates arising from (primarily anharmonic) coupling of nearly isoenergetic normal mode vibrations (vide infra). For the case of randomly distributed energy levels and coupling strengths of a set of zero order vibrational states, it was shown[30] that the IVR rate is given by a golden-rule-type relation,

$$1/\tau_{IVR} \cong 2\pi/\hbar[(\delta V)^2 \rho] \qquad (11)$$

where $(\delta V)^2$ is the variance in coupling strengths, as long as the average spacing of vibrational states is small compared to δV. If a constant variance is assumed, eq 11 predicts a linear increase in IVR rate with ρ, the vibrational density of states. In Figure 15, we show a direct count of ρ *vs* E_{ex} in harmonic approximation,[31] based on the same frequency set described previously for the thermal energy calculations.[28,29] (Given this $\rho(E)$ and assuming symmetry-restricted coupling to a single one of the four C_{2h} symmetry species, δV in the vicinity of 1250 cm^{-1} is found to range from 0.4 to 0.5 GHz, on the same order of magnitude as previously calculated values.[6]) On the basis of that calculation and eq 11, the predicted extrapolation of the IVR lifetime is shown by the solid line in Figure 16. The increase in ρ from 570/cm^{-1} at 1280 cm^{-1} to 7900/cm^{-1} at 1830 cm^{-1} translates into a predicted decrease in τ from 35 to 2.5 ps. By 2250 cm^{-1}, the predicted lifetime is 420 fs, falling

Femtosecond Real-Time Probing of Reactions

J. Phys. Chem., Vol. 100, No. 29, 1996 **11929**

another order of magnitude for every additional $650-700$ cm^{-1}. These estimates are, of course, subject to great uncertainty, but can be assumed to give some indication of the trend.

In addition to the intrinsic molecular rate considered above, the initial state preparation must be considered as a factor of fundamental importance in IVR dynamics. The spectral coherence width of the pump pulse determines the energy spread of molecular eigenstates that may be coherently excited to form the initial superposition state. This spread, in turn, limits the maximum rate at which the superposition will dephase, or lose the character of the initial state. If the spread of coupled levels is much greater than the pump bandwidth, then the IVR rate will be limited by the pump pulse and will not be an intrinsic characteristic of the molecule. This limitation is distinct from the temporal resolution limitation associated with the instrument response, which depends on the probe (or detection) as well. In the case that a fast pump pulse prepares a state that undergoes fast IVR, but the instrument response is slow, convolution will severely damp the apparent amplitude of the fast component and the deconvoluted lifetime will approach 0. An example would be picosecond fluorescence, where the pulses are short and the instrument response is limited by the fluorescence detection.

At excess energies above 4000 cm^{-1}, the IVR lifetime estimated by eq 11 falls below 1 fs (see Figure 16). Since the frequency bandwidth corresponding to such a dephasing rate exceeds 5000 cm^{-1}, the assumption in ref 30 of randomly distributed zeroth-order vibrational states clearly no longer holds (Figure 15), and the validity of the extrapolation must break down before this point. This is not a significant concern over a range of plus or minus a few hundred cm^{-1}, however, and random coupling over such a range would give IVR times in the vicinity of 10 fs. This would suggest that the fast component lifetimes of $280-650$ fs measured at much higher state densities in the energy range $5300-6500$ cm^{-1} must be pulse limited and not reflections of the complete molecular IVR rate. This would also account for the variation in lifetimes measured, depending on variable pulse lengths and coherence bandwidths. The same conclusion may be drawn about the 2 ps fast components observed in ref 16, both because the lifetimes measured there remained constant over an energy range of 2600 cm^{-1} and because a shorter lifetime (780 fs) was measured with the order of magnitude shorter pulses used here, even at the lowest energy of the range (1830 cm^{-1}) (see Figure 14a).

On the other hand, the 780 fs lifetime appears to be a reliable measurement of the IVR process at 1830 cm^{-1}, since (1) the 310 nm pump pulse provided by frequency doubling the direct CPM output is expected to provide a coherent bandwidth greatly exceeding that needed to yield a 780 fs decay and (2) the total instrument response indicated by the rise of the transient is $\sim$330 fs, short enough to avoid the question of adequate temporal resolution. From this it may be deduced that over an interval of 550 cm^{-1}, from 1280 to 1830 cm^{-1}, the golden rule extrapolation falls behind the true increase in IVR rate by a factor of $\sim$3.2. This difference may represent systematic changes in δV or the influence of anharmonicity on ρ. The effective density of states may also increase faster than predicted if the symmetry restriction on coupling breaks down with increasing energy.

By assuming that this deviation represents a systematic effect, we may make a revised estimate of the IVR rate as a function of energy. For example, since $\log(\rho(E))$ is approximately linear, it is reasonable to add a linear term to the energy dependence of $\log(1/\tau_{IVR})$ to bring the calculation into agreement with experiment at 1280 and 1830 cm^{-1}. This adjustment is

represented by the dashed line in Figure 16. The predicted IVR lifetime falls to $\sim$54 fs at 2250 cm^{-1}, in the range of the fast lifetimes measured at that energy, and thereafter drops an order of magnitude every 400 cm^{-1}. In this estimate, the lifetime would reach the 1 fs range below 3000 cm^{-1}. This result suggests that even the 60 fs rise at 3120 cm^{-1} may be pulse limited.

According to the kinetic model presented in section III.1, the fast to slow amplitude ratio is expected to depend on the relative cross section for probing the initial and redistributed states. Although these cross sections include Franck$-$Condon factors, and thus depend on the pump wavelength as well, this complication will be ignored here. From the fluorescence depletion results, the one-photon cross sections may be derived. We find $\beta < 0.5$ for a 612 nm probe, and $\beta \cong 0.5$ for a 583 nm probe. Assuming from Franck$-$Condon considerations that downward depletion is negligible, $\beta \leq 0.5$ means that the cross section of the $S_4' \leftarrow |d\rangle$ S_1 transition is greater than or equal to that of $S_4 \leftarrow |b\rangle$ S_1, where the prime is used to indicate that different subsets of the S_4 vibrational manifold are reached from $|b\rangle$ and $|d\rangle$ (see Figure 3). For ionization, β represents an effective total ionization cross section, and it is found to be ≥ 0.5 for the 612 nm probe, and > 0.5 for a 580 or 583 nm probe. However, the signal from the two-step probe process actually depends on two cross sections, that for $S_4 \leftarrow S_1$ and that for $S^+ \leftarrow S_4$. The fact that β goes up at both probe wavelengths when changing from depletion to ionization requires that the second probe photon ionizes the S_4 levels populated from $|b\rangle$ more efficiently than those from $|d\rangle$ or, equivalently, that the cross section for probing $|c\rangle \leftarrow S_4$ is several times higher than for probing $|g\rangle \leftarrow S_4'$.

The above reversal of relative cross sections between the two steps of the two-photon transition to the ion is confirmed in another way, without consideration of the depletion results. The fast to slow amplitude ratio of ionization transients has been observed in some cases to increase with probe intensity. This same observation concerning amplitude ratios was made for the biexponential decays of ref 16, where it was demonstrated that the amplitude of the slow component ($|g\rangle \leftarrow |d\rangle$) reaches saturation while the fast component ($|c\rangle \leftarrow |b\rangle$) continues to grow with probe power. At the same time, the observation of biexponential decays corresponds to $\beta > 0.5$, or to a larger total cross section for probing $|b\rangle$ than for probing $|d\rangle$. This would be inconsistent with the kinetic model were the ionization a single photon process, since the transition with the larger cross section would reach saturation first. Thus, we see again that the relative cross sections of the two-photon transition must be reversed between the two steps. In this case, saturation occurs in $S_4' \leftarrow |d\rangle$ S_1 before it occurs in $S_4 \leftarrow |b\rangle$ S_1, while the total cross section for ionization is higher from $|b\rangle$ than from $|d\rangle$ because the strong bias in the second photon step more than compensates for the smaller absorption from $|b\rangle$.

Since ν_{25}, the phenyl$-$ethylene symmetric in-plane bend, is the only *trans*-stilbene vibrational mode showing a long progression in $S_1 \leftarrow S_0$ absorption, the $|b\rangle$-type states are expected to be characterized by fairly large amplitude motions in that bend. This should be the principal distinction between $|b\rangle$ and $|d\rangle$ states, the latter consisting predominantly, from density of states considerations, of combination bands with extensive excitation of the low-frequency out-of-plane bends and torsions of the phenyl rings. The observation that $|b\rangle$ and $|d\rangle$ have different saturation thresholds and that S_4 and S_4' have distinct ionization cross sections must also be traceable to these differences in mode character and hence to differing Franck$-$Condon factors due to structural differences between the excited
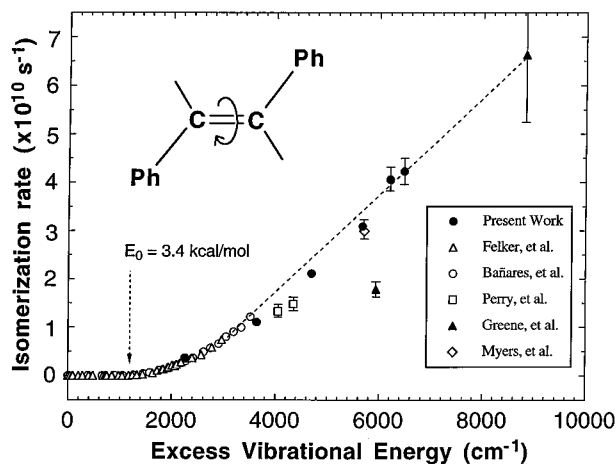
Figure 17. Nonradiative, or isomerization, decay rate of *trans*-stilbene *vs* excess energy. The open squares were obtained by Felker et al.[3,12] The open circles are the result of work by Bañares et al.[13] Both of these sets of data were obtained using supersonic jets. Previous bulb measurements by Perry et al.[16] at room temperature, Greene et al.[17] at 380 K, and Meyers et al.[18] at 463 K are also shown (see text). The excess energies are computed from the photon energy and the average thermal vibrational energy. The solid circles represent the current work at room temperature using the ionization cell. Error bars for data from other sources are as given in the original publication. For the lowest energy data, the errors are smaller than the plot symbols. For the present work, error bars are given where multiple measurements were made and represent the range of values obtained.

states. However, the multidimensional nature of the problem makes it difficult to link such effects to any specific structural characteristics of the states.

IV.4. Isomerization Rates. Applying the kinetic model of section III to the data presented above, we extract the rates of isomerization simply from the measured lifetimes of the slow components. The radiative rate of *trans*-stilbene is in the nanosecond range[12] and has essentially no influence at these high energies; we correct for its contribution. The derived rates are plotted as a function of the excess energy in Figure 17, along with results of previous studies. All data have been plotted on a common energy axis by accounting for differing thermal energies. Error bars for the present study indicate the range of derived rates when repeated measurements are available. For other data, error bars are as reported in the cited reference.

Below an excess energy of 3500 cm^{-1}, the isomerization rate is well studied. However, previous measurements left some ambiguity as to the trend of the rates in the higher energy range. The isomerization rates measured in the present study are expected to be most accurate from 3600 to 6500 cm^{-1}. Figure 17 shows that these fall near a straight line connecting the low-energy results to the ref 17 data point near 9000 cm^{-1} and are in good agreement with the single rate measured by fluorescence up-conversion in ref 18. In contrast, the point near 6000 cm^{-1} from the former work[17] falls well below this line. While the sample temperature may be expected to affect the thermally averaged rate that is measured, the agreement of the data from ref 18 with the present results, despite 3000 cm^{-1} of additional average thermal vibrational energy, supports the validity of the treatment of thermal and photon energies as effectively equivalent. This effective equivalence is also seen in the good agreement between bulb and molecular beam measurements in the low-energy region[12,16] and is shown by calculations to hold to good approximation for a simple shift of the Boltzmann distribution without distortion upon transfer of population from S_0 to S_1.[32]

Since IVR is seen to be much faster than isomerization, many studies have attempted to model the *trans*-stilbene isomerization reaction by statistical theories, assuming complete randomization of vibrational energy among energetically accessible modes. The first such efforts[33,14] employed RRK theory, which gives the following expression for the reaction rate:

$$k(E) = \nu \left(\frac{E - E_0}{E} \right)^{s-1} \tag{12}$$

where ν is the frequency of the reaction coordinate, E_0 is the barrier height, and s is an effective number of vibrational modes. This expression was found to give a good approximation to the measured excess energy dependence of the *trans*-stilbene isomerization rate below 2700 cm^{-1}. The curves defined by the two sets of proposed values for ν, E_0, and s (3.2×10^{10} s^{-1}, 900 cm^{-1}, and 6,[33] or 4.8×10^{10} s^{-1}, 700 cm^{-1}, and 9[14]), with the neglect of zero-point energy, are virtually indistinguishable in that range, but both begin to fall below the experimental data as shown in Figure 17 by 3000 cm^{-1}. Given that ν is the limiting value of the RRK rate at high E, it is evident that a higher value of ν is necessary to reproduce the experimental rates. With higher ν and the inclusion of zero-point energy as a fourth parameter, the functional form of the rate curve could be fit to higher energy, but because the interpretation of the fit parameters in terms of physical properties of the system is at best qualitative, the value of these comparisons is limited.

RRKM theory relates the statistical reaction rate directly to ρ and $\rho^\dagger$, the quantum mechanical vibrational state densities in the reactant and transition state, respectively, and is thus more amenable to quantitative interpretation and comparisons. The RRKM rate is given by

$$k(E) = \frac{\int_0^{E-E_0} \rho^\dagger(E_v^\dagger)\, dE_v^\dagger}{h\rho(E)} = \frac{N^\dagger(E - E_0)}{h\rho(E)} \tag{13}$$

where $E_v^\dagger$ is the vibrational energy in the bound coordinates of the transition state, and $N^\dagger$ is the total number of vibrational states in the transition state whose energies lie lower than the reactant energy E. In the case of *trans* stilbene, it has been found that, if the transition state frequencies are unchanged from the reactant, RRKM theory predicts rates that are much higher than the measured rates for the isolated molecule.[12,34] On the other hand, the thermal average of these RRKM predicted rates is much closer to observed low viscosity solution rates than is the thermal average of the measured molecular beam rates.[12] Since the vibrational frequencies in the transition state are determining parameters in RRKM calculations and these are not directly measurable, a variety of different assumptions about the frequencies can be made to adjust the theory to either the isolated molecule or the solution experimental results, but the incompatibility of the two will persist without some additional adjustment in the assumptions of the theory.

Troe[32] has shown that by using a reaction coordinate frequency of 88 cm^{-1} and adjusting the vibrational frequencies of the 15 bound modes involving motion of the ethylenic double bond upward by a factor of 1.2 from the reactant to the transition state, good agreement can be achieved between RRKM calculations and measured rates up to $E_{ex} \cong 4000$ cm^{-1}. Solvation-induced changes in E_0, for example, are then proposed to explain the solution results.[32,35]

Alternatively,[3] with little change in frequencies, nonadiabatic effects in the isolated molecule can be invoked at the avoided crossing between electronic states that forms the reaction barrier. The RRKM calculation must then be modified to account for

the Landau−Zener curve-crossing probability, P, that a nona-diabatic crossing will prevent reaction from occurring. P is a function of velocity, v, along the reaction coordinate at the transition state, which approaches unity at high v:[3]

$$P(v) = \exp\left[-\frac{\pi}{2\hbar}\frac{\Delta^2}{|F_1 - F_2|}\frac{1}{v}\right] \quad (14)$$

Here Δ is the energy splitting of the adiabatic surfaces at the avoided crossing, and F_1 and F_2 are the slopes of the diabatic curves there. The nonadiabatic RRKM rate is found by scaling the state count by the adiabatic passage probability $(1 - P)$:

$$k(E) = \frac{\int_0^{E-E_0}(1 - P(v))\rho^\dagger(E_v^\dagger)\,dE_v^\dagger}{h\rho(E)} \quad (15)$$

where v is a function of $E_v^\dagger$ through energy conservation.[3] With reasonable potential parameters in eq 14, the isomerization rates of both *trans*-stilbene and perdeuterated *trans*-stilbene up to $E_{ex} = 3000$ cm^{-1} are well fit by nonadiabatic RRKM calculations using the same frequencies in reactant and transition state and a reaction coordinate frequency of 400 cm^{-1}.[3] A rate increase in solution, as observed, can then follow from solvent-induced reduction in v, which shifts eq 15 toward the fully adiabatic limit $(P = 0)$ given by eq 13.

Both of these approaches have been reexamined by Negri and Orlandi[36] by carrying out RRKM calculations for two different transition states, A and B, with vibrational frequencies computed by the semiempirical QCFF/PI Hamiltonian, with and without inclusion of doubly excited configurations in the configuration interaction, for A and B, respectively. The results for *trans*-stilbene and several of its isotopomers were compared to experimental molecular beam rates in the low-energy range $(E_{ex} < 3000$ cm$^{-1})$.[3,15] For the A transition state, the barrier results from an avoided crossing and the effect of nonadiabaticity must be considered, while the B transition state involves only one electronic state surface and, therefore, only a standard fully adiabatic treatment is required. By optimizing E_0 for each set of calculations, and the factor $\gamma = \Delta^2/|F_1 - F_2|$ for the nonadiabatic calculation, reasonably good agreement with experiment was achieved for both A and B transition states. As discussed below, Negri and Orlandi drew a distinction between the two alternative models only on the basis of arguments derived from comparison with rates measured in solution.[36]

Given the much greater energy range represented by the data in Figure 17, we have used the transition state frequencies and parameters derived in ref 36, without further adjustment, to extend the calculation to higher energy. The resulting rate curves are plotted with the data in Figure 18. The rates for the A transition state have been calculated nonadiabatically with a barrier of 1200 cm^{-1}, as required to match the data, but also by standard adiabatic RRKM theory, to again illustrate the importance of nonadiabaticity. A barrier of 1250 cm^{-1} is used for the B transition state calculation.[36] The trend to higher energy of the calculated rates for both the B transition state and nonadiabatic A transition state continues to match the trend of the data very closely, becoming almost linear above 5000 cm^{-1}. Although the curves depend on adjustable parameters, which have not been reoptimized here, they are fairly tightly constrained by the requirement of fitting three other isotopomers of *trans*-stilbene besides the perprotio species.[36]

To see if these two mathematical models continue to agree closely or diverge with increasing energy and to get a better overall picture of the origin of the linear behavior, the calculations were extended as shown in Figure 19. The data
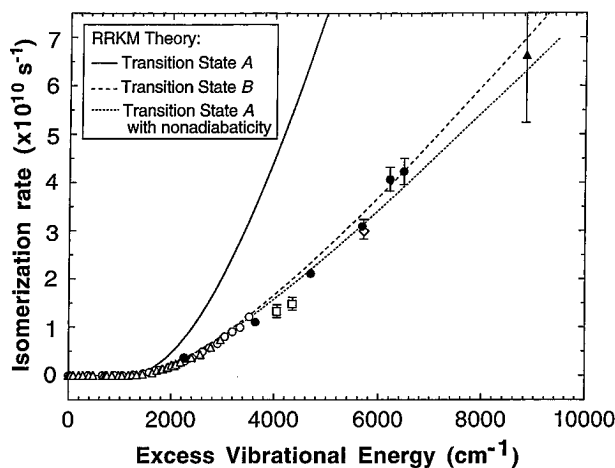

Figure 18. Comparison of measured isomerization rates of *trans*-stilbene with theoretical model calculations. The experimental data are as in Figure 14, with the measurement near 6000 cm^{-1} from ref 17 removed since it is in poor agreement with other data near the same excess energy. The theoretical curves represent RRKM rates calculated for transition states and other parameters given in ref 36. Standard calculations, in which the barrier crossing is treated as fully adiabatic, are given for two transition states (designated as A and B). The third calculation is also based on the A transition state but includes a degree of nonadiabaticity in the crossing.
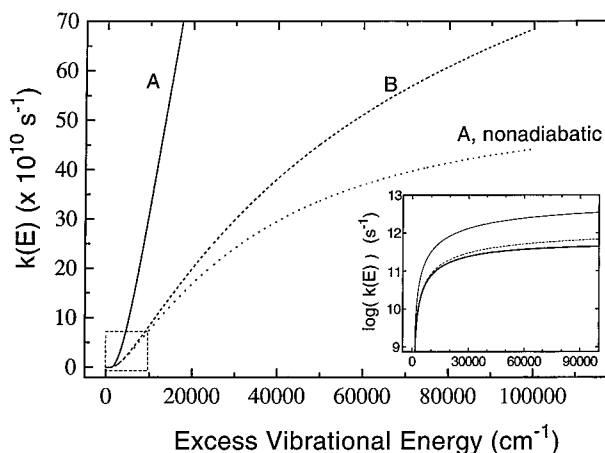

Figure 19. Extension of the three theoretical curves of Figure 18 to higher energy. The dashed box at the origin indicates the range of data contained in Figure 18. See Figure 18 caption for details. A log plot for the same curves is shown in the inset.

within the small dashed box at the origin are those shown in detail in Figure 18. We see from Figure 19 that the near linear behavior arises from an inflection in the rate curves and extends to $E_{ex} \approx 17\,000$ cm^{-1}. The two relevant curves separate only very gradually, differing by less than 20% until $E_{ex} = 27\,000$ cm^{-1}. It is therefore reasonable to conclude that, in this case, extending the rate measurements to higher energy will not be a useful strategy for distinguishing the two theoretical models, even if the model calculations could be expected to yield quantitative correspondence to the actual physical system behavior at very high energies. In practice, since this is not the case and since the two models predict rates that remain within a factor of 2 at all energies, even accurate experimental rates at high energies would not provide a compelling argument for either model.

Although both models give satisfactory fits to the gas phase rates, Negri and Orlandi concluded that the nonadiabatic model of Felker et al.,[3] embodied in the A transition state calculations, has advantages in explaining the acceleration in measured isomerization rates from gas phase to solution.[36] First, it is clear

from Figures 18 and 19 that, if nonadiabaticity is reduced for the *A* transition state, a large rate increase is possible. Negri and Orlandi found that the thermal averages increased by roughly a factor of 3 when the rates were treated adiabatically. This increased adiabaticity can be attributed, as did Felker et al.,[3] to solvent viscosity slowing the velocity along the twisting coordinate. The thermally averaged adiabatic rates for the *A* transition state are still found by Negri and Orlandi to be smaller than the rates in low-viscosity solution. This discrepancy can be eliminated by a lowering of the transition state by solvation, that is, by a decrease in E_0, for which effect a body of experimental evidence exists.[35,37] Negri and Orlandi point out that such a solvation effect on E_0 is also more likely to be associated with the *A* transition state, in which the barrier is formed by an avoided crossing of two electronic state surfaces.[36]

Molecular dynamics of the *trans* to *cis* configurational change should provide a more direct theoretical description of the twisting process. Bolton and Nordholm[38] have provided a microscopic picture of the intramolecular energy flow using model potentials and trajectory calculations. They qualitatively reproduce the experimentally observed restricted, quasi-periodic IVR.[6] They also found, from these classical trajectory calculations, that a bottleneck to IVR may persist. Such behavior of IVR has an effect on rates and the validity of statistical models, as discussed in refs 3, 14, 38, and elsewhere,[2] and is important in the low-energy regime. As discussed in section IV.3, measured IVR rates above the isomerization barrier are larger than the isomerization rate. Vachev et al.[39] have reported quasi-classical molecular dynamics simulations of the isomerization of both *cis* to *trans* and *trans* to *cis*. Nonadiabatic coupling to the ground state was included in the calculations for deactivation of the phantom state. For the *trans* to *cis* process, they reproduce the picosecond time scale, in contrast to the *cis* to *trans* dynamics, which takes place on the femtosecond time scale. These results are determined largely by inclusion of a bonding potential of chemical strength between a specific pair of carbon atoms located on opposite phenyl rings. Future MD calculations will undoubtedly aim at refining the potential and including quantum effects.

V. Conclusions

In this work, femtosecond multiphoton ionization and fluorescence depletion techniques have been applied to the study of three dynamic processes in the *trans*-stilbene excited state: time-dependent alignment, intramolecular vibrational energy redistribution, and isomerization. The results have been compared with theoretical models, each of which has been applied previously to earlier *trans*-stilbene measurements of lower temporal resolution. The time scale of rotational dynamics of the isolated molecule in the room temperature vapor, as reflected in the polarization anisotropy decay, is fully resolved and found to correspond closely to the predictions of rotational coherence theory. After extraction of alignment effects, fast and slow rate components in the transients reveal two nonradiative population transfer processes, which can be analyzed by a kinetic model. The intrinsic molecular IVR rate appears to roughly follow an extrapolation of a golden rule relation from the picosecond to the femtosecond time domain, becoming unmeasurable at excess energies above 2250 cm^{-1}, while experimental IVR decays from pulse limited state preparation are observable to high energy. Absorption cross sections are found to differ widely between initial and redistributed states in S_1 and in the corresponding S_4 states. The energy dependence of the isomerization rate is measured up to 6500 cm^{-1}, showing good agreement with the trends predicted by the application of adiabatic and nonadiabatic

RRKM theories to model systems that had previously been adjusted to match isomerization data below 3000 cm^{-1}.

In future, we will extend the present studies to the effect of structural changes[13] on IVR and rates and compare with very recent work on similar systems by the Rettig group.[40]

Appendix

The kinetic model of Figure 3 is a specialized case of the following more simplified scheme, with initial state **A** going to product **P**:
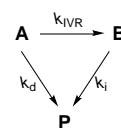
where k_d is the rate constant for direct product formation and k_i is the rate constant for indirect product formation, following IVR to **B**. The general solution for the populations of **A** and **B** for $t > 0$, assuming $n_A(0) = n_0$ and $n_B(0) = 0$, is

$$n_A(t) = n_0 \exp(-(k_{IVR} + k_d)t) \tag{A1}$$

$$n_B(t) = \frac{n_0 k_{IVR}}{(k_{IVR} + k_d) - k_i}[\exp(-k_i t) - \exp(-(k_{IVR} + k_d)t)] \tag{A2}$$

The initial state decays at a total rate $k_{IVR} + k_d$ and **B** rises with the *faster* of the rates, $(k_{IVR} + k_d)$ or k_i, and decays with the slower of the two, since the relative size of these two rates determines the sign of the prefactor. If there are no reverse rates and the population of **P** is not monitored, it is irrelevant whether or not the channels characterized by k_d and k_i terminate on a common product state.

When both **A** and **B** are monitored, the total signal $S(t)$ will be a sum in which the relative amplitudes of the two contributions may be represented by arbitrary positive coefficients a and b:

$$S(t) = n_0\left\{a \exp(-(k_{IVR} + k_d)t) + \frac{b k_{IVR}}{(k_{IVR} + k_d) - k_i} \times \right.$$
$$\left. [\exp(-k_i t) - \exp(-(k_{IVR} + k_d)t)]\right\} \tag{A3}$$

Note that, if $(k_{IVR} + k_d) > k_i$, the amplitudes of the $(k_{IVR} + k_d)$ components are of opposite sign, and each of the behaviors shown in Figure 4 may occur, depending on a and b. If $(k_{IVR} + k_d) < k_i$, however, the amplitudes of the $(k_{IVR} + k_d)$ components are both positive, and these contribute to the long time decay. The amplitude of the single k_i component is ≤ 0, so there can be no short time decay, only a rise or partial rise, or no rise if $b = 0$. Thus, whatever the size of b, the signal *always* has only one decaying component.

We can now adapt the above result to find the populations of $|b\rangle$ and $|d\rangle$ in the kinetic model of Figure 3, without imposing the restrictions of eq 1. We need only add back the fluorescence

Femtosecond Real-Time Probing of Reactions

J. Phys. Chem., Vol. 100, No. 29, 1996 **11933**

channels, f_d and f_b, for completeness. For $t > 0$:

$$n_b(t) = n_0 \exp(-(k_{IVR} + k_b + f_b)t) \qquad (A4)$$

$$n_d(t) = \frac{n_0 k_{IVR}}{(k_{IVR} + k_b + f_b) - (k_{iso} + f_d)}[\exp(-(k_{iso} + f_d)t) - \exp(-(k_{IVR} + k_b + f_b)t)] \quad (A5)$$

Here, an additional decay channel from $|b\rangle$, at rate k_b, has also been included. This may, for example, represent direct isomerization without IVR, in analogy with k_d above, but its role in the temporal evolution of n_b or n_d is indistinguishable from that of f_b. In this respect, k_{IVR} is also indistinguishable from $k_b + f_b$ except in its role as an amplitude factor in n_d. When monitoring both $|b\rangle$ and $|d\rangle$ populations, the relative amplitudes of the two contributions will be determined by their respective probe cross sections, represented by the parameter β, as discussed in section III.1.

We may use eqs A4 and A5 to see the explicit form of the total ion signal, for example, if, in violation of eq 1a, $k_{iso} + f_d$ were greater than $k_{IVR} + k_b + f_b$. Changing the prefactor in eq A5 to $n_0 k_{IVR}/[(k_{iso} + f_d) - (k_{IVR} + k_b + f_b)] \equiv n_0 c$, which is now positive, and defining $k_{tot} = k_{IVR} + k_b + f_b$, the total ion signal becomes

$$M_{ion}(t) = n_0 \alpha \sigma_{0i}\{\beta_i \exp(-k_{tot}t) + c(1 - \beta_i)[\exp(-k_{tot}t) - \exp(-(k_{iso} + f_d)t)]\} \quad (A6)$$

or, by combining terms,

$$M_{ion}(t) = n_0 \alpha \sigma_{0i}\{[c(1 - \beta_i) + \beta_i] \exp(-k_{tot}t) - c(1 - \beta_i) \exp(-(k_{iso} + f_d)t)\} \quad (A7)$$

(For $c = -1$, eq 4b is recovered.) Since we are assuming now that c is positive and $0 < \beta_i < 1$, we find, as expected, that the resulting transient *always* has only one decaying component (of rate k_{tot}), and for $\beta_i < 1$, it also has a fast rise of rate $(k_{iso} + f_d)$. The rise may be partial, as in Figure 4c, or full if $\beta_i = 0$. Thus, the ionization transients observed to have two decaying components can be described by a kinetic model like that of Figure 3 only when the fast component is associated with IVR, in accord with the interpretation in section IV.3.

References and Notes

(1) Saltiel, J.; Sun, Y.-P. In *Photochroism-Molecules and Systems*; Dürr, H., Bouas-Laurent, H., Eds.; Elsevier: Amsterdam, 1990; p 64.
(2) Waldeck, D. H. *Chem. Rev.* **1991**, *91*, 415.
(3) Felker, P. M.; Zewail, A. H. *J. Phys. Chem.* **1985**, *89*, 5402.
(4) Orlandi, G.; Siebrand, W. *Chem. Phys. Lett.* **1975**, *30*, 352.
(5) Taven, P.; Schulten, K. *Chem. Phys. Lett.* **1978**, *56*, 200.
(6) Felker, P. M.; Lambert, W. R.; Zewail, A. H. *J. Chem. Phys.* **1985**, *82*, 3003.
(7) Scherer, N. F.; Shepanski, J. F.; Zewail, A. H. *J. Chem. Phys.* **1984**, *81*, 2181.
(8) Baskin, J. S.; Felker, P. M.; Zewail, A. H. *J. Chem. Phys.* **1987**, *86*, 2483.
(9) Baskin, J. S.; Zewail, A. H. *J. Phys. Chem.* **1989**, *93*, 5701.
(10) Scherer, N. F.; Khundkar, L. R.; Rose, T. S.; Zewail, A. H. *J. Phys. Chem.* **1987**, *91*, 6478.
(11) Syage, J. A.; Lambert, Wm. R.; Felker, P. M.; Zewail, A. H.; Hochstrasser, R. M. *Chem. Phys. Lett.* **1982**, *88*, 266.
(12) Syage, J. A.; Felker, P. M.; Zewail, A. H. *J. Chem. Phys.* **1984**, *81*, 4706.
(13) Bañares, L.; Heikal, A. A.; Zewail, A. H. *J. Phys. Chem.* **1992**, *96*, 4127.
(14) Majors, T. J.; Even, U.; Jortner, J. *J. Chem. Phys.* **1984**, *81*, 2330.
(15) Courtney, S. H.; Balk, M. W.; Phillips, L. A.; Webb, S. P.; Yang, D.; Levy, D. H.; Fleming, G. R. *J. Chem. Phys.* **1988**, *89*, 6697.
(16) Perry, J. W.; Scherer, N. F.; Zewail, A. H. *Chem. Phys. Lett.* **1983**, *103*, 1.
(17) Greene, B. I.; Hochstrasser, R. M.; Weisman, R. B. *Chem. Phys.* **1980**, *48*, 289.
(18) Meyers, A. B.; Holt, P. I.; Pereira, M. A.; Hochstrasser, R. M. *Chem. Phys. Lett.* **1986**, *132*, 585.
(19) Rosker, M. J.; Dantus, M.; Zewail, A. H. *J. Chem. Phys.* **1988**, *89*, 6113.
(20) Khundkar, L. R.; Zewail, A. H. *Annu. Rev. Phys. Chem.* **1990**, *41*, 15, and references therein.
(21) Herek, J. L.; Pedersen, S.; Bañares, L.; Zewail, A. H. *J. Chem. Phys.* **1992**, *97*, 9046.
(22) Semmes, D. H.; Baskin, J. S.; Zewail, A. H. *J. Chem. Phys.* **1990**, *92*, 3359.
(23) see Felker, P. M.; Zewail, A. H. In *Femtochemistry*; Manz, J., Wöste, L., Eds.; VCH: Weinheim, **1995**, and references therein.
(24) Champagne, B. B.; Pfanstiel, J. F.; Plusquellic, D. F.; Pratt, D. W.; Herpen, W. M.; Meerts, W. L. *J. Phys. Chem.* **1990**, *94*, 6.
(25) Baskin, J. S.; Zewail, A. H. *J. Phys. Chem.* **1994**, *98*, 3337.
(26) Gordon, R. G. *J. Chem. Phys.* **1965**, *43*, 1307.
(27) Felker, P. M.; Zewail, A. H. *J. Chem. Phys.* **1987**, *86*, 2460.
(28) Warshel, A. *J. Chem. Phys.* **1975**, *62*, 214.
(29) Urano, T.; Maegawa, M.; Yamanouchi, K.; Tsuchiya, S. *J. Phys. Chem.* **1989**, *93*, 3459.
(30) Tric, C. *Chem. Phys.* **1976**, *14*, 189.
(31) Beyer, T.; Swinehart, D. F. *Commun. Assoc. Comput. Machin.* **1973**, *16*, 379.
(32) Troe, *J. Chem. Phys. Lett.* **1985**, *114*, 241.
(33) Zewail, A. H. *Laser Chem.* **1983**, *2*, 55.
(34) Khundkar, L. R.; Marcus, R. A.; Zewail, A. H. *J. Phys. Chem.* **1983**, *87*, 2473.
(35) Schroeder, J.; Schwarzer, D.; Troe, J.; Voss, F. *J. Chem. Phys.* **1990**, *93*, 2393.
(36) Negri, F.; Orlandi, G. *J. Phys. Chem.* **1991**, *95*, 748.
(37) Heikal, A. A.; Chong, S. H.; Baskin, J. S.; Zewail, A. H. *Chem. Phys. Lett.* **1995**, *242*, 380.
(38) Bolton, K.; Nordholm, S. *Chem. Phys.* **1996**, *203*, 101.
(39) Vachev, V. O.; Frederick, J. H.; Grishanin, B. A.; Zadkov, V. N.; Koroteev, N.I. *J. Phys. Chem.* **1995**, *99*, 5247.
(40) Monte, Ch.; Hoffmann, K.; Siemoneit, A.; Staak, M.; Zimmermann, P.; Rettig, W.; Lapouyade, R. Work to be published.